A comprehensive model of plastic wear based on the discrete element method

Powder Technology 410 (2022) 117864

Contents lists available at ScienceDirect

Powder Technology

journal homepage: www.journals.elsevier.com/powder-technology

A comprehensive model of plastic wear based on the discrete element method

R. Capozza *, K.J. Hanley

School of Engineering, Institute for Infrastructure and Environment, The University of Edinburgh, Thomas Bayes Road, Edinburgh, EH9 3JL, United Kingdom

HIGHLIGHTS

- A unified wear model has been developed for both impact and scratching scenarios.
- An abradable surface is discretised using small spheres in DEM.
- The change in surface profile due to wear is captured by displacing the spheres.
- Simulations show a qualitative agreement with literature data.

GRAPHICAL ABSTRACT

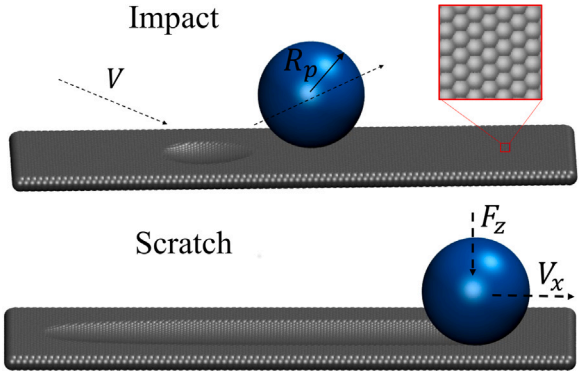

ARTICLE INFO

Keywords:
Abrasion
Erosion
Hardness
Archard model
Finnie model

ABSTRACT

A comprehensive computational model of wear has been developed. It simulates the wearing of a surface due to both scratching with a rigid indenter or normal/oblique impact of a rigid projectile. A group of spheres models the surface, characterised by the hardness. When the pressure overcomes a threshold, spheres are displaced to account for the change in surface profile. In the case of impact, the wear volume grows with the velocity and reaches a maximum between 0 and 90°. In the case of scratching, the dependence of the worn volume on the normal load is linear in a limited range of loads (Archard's law) and transitions to a non-linear behaviour with the increase of load. Energy dissipation is naturally included in the model without additional parameters. This conceptually simple approach can easily be extended to model a variety of industrial applications and potentially predict wear patterns under varying scenarios.

1. Introduction

Wear is the process of material removal from surfaces. It has countless consequences in nature and in many industrial applications [1] such as oil production and refining [2] and mineral processing and mining [3]. Wear affects the design of engine components [4] and industrial equipment for slurry handling [5] and pneumatic conveying [6], among many others. Wear has major effects, not only at the single-particle level (e.g., change of angularity) but also at the macroscale. For example, the presence of abrasive wear reduces the peak friction angle of railway ballast [7]. Because of abrasion the particle morphology changes [8] and the inter-particle friction coefficient cannot be considered constant [9–11], which is standard practice in discrete element method (DEM) simulations.

The importance and complexity of wear has resulted in the development of many models [12,13]. In many cases wear is simply estimated from energy and forces [14] and, when simulated explicitly, the model used is application-dependent [15,16]. This is the case for wear due to both impact and scratching for which the Finnie [1] and Archard [17]

* Corresponding author.
E-mail address: rcapozza@exseed.ed.ac.uk (R. Capozza).

https://doi.org/10.1016/j.powtec.2022.117864
Received 27 June 2022; Received in revised form 7 August 2022; Accepted 18 August 2022
Available online 24 August 2022

Nomenclature

$\Delta\theta$	Deviation angle
δE_i^k	Energy dissipated by wear at surface sphere i during time-step k
μ	Friction coefficient
μ_a	Tangential to normal force ratio
ν	Poisson's ratio
ϕ_i	Angle between the vertical axes and the line joining the particle's centre and the sphere i
θ	Impact angle
θ_r	Post-impact rebound angle of the projectile
A	Surface area
A_x	Contact area orthogonal to the scratching direction
A_z	Area of contact orthogonal to the vertical load
A_{ind}	Indented area
a_i	Effective area per sphere accounting for the increased area due to surface indentation
A_{LB}	Load-bearing area
A_{LB}^L	Lateral load-bearing area
A_{LB}^V	Vertical load-bearing area
a_s	Area per sphere (flat surface), i.e., $a_s = \frac{A}{N}$
COR	Restitution coefficient
dt	Simulation time increment
dx	Calculated displacement increment for a surface sphere due to a lateral force
dz	Incremental displacement of a sphere comprising the surface in the vertical direction due to a normal force
$dz_{x,i}$	Incremental displacement of a sphere comprising the surface in the vertical direction due to a lateral force
E	Young's modulus
E_i^k	Total energy dissipated by wear by time-step k
F_{ext}	External force applied to indenter
$F_{x,i}$	Lateral component of force applied to a sphere
$F_{z,i}$	Vertical component of force applied to a sphere
H	Hardness of the surface
h	Indentation depth
H_l	Shear hardness; $H_l = \mu_a H$
h_i	Sphere-dependent indentation depth
i_L	Per-sphere lateral flow index
i_V	Per-sphere vertical flow index
L	Length of the discretised surface
m	Mass of the indenting particle or projectile
N	Number of surface spheres
n_f	Number of surface spheres in the flow regime
P_x	Lateral pressure
P_z	Vertical pressure
r	Effective radius; $r = r_s + R_p$
R_p	Radius of spherical indenter (scratching) or projectile (impact)
r_s	Radius of each sphere comprising the discretised surface
S	Width of the discretised surface
V	Velocity
V_r	Post-impact rebound velocity of the projectile
V_x	Lateral component of velocity
V_z	Vertical component of velocity
W_V	Wear volume
z_0	Initial vertical coordinate of the surface spheres when the surface is flat

models, respectively, are widely used. Both of these models neglect the bulk of the eroded material and consider hardness as the only surface property.

The Finnie model applies to the impact of a particle with a surface. The volume removed depends on the impact angle θ and is estimated based on a number of assumptions. The area of contact is assumed circular and the ratio of the tangential force to the normal force on the particle is taken as a constant $\mu_a < 1$ [18,19]. A consequence of this last assumption is that, during the impact, the force needed to remove a volume element along the tangential direction is smaller than along the normal direction, and the volume removed has a maximum for $0 < \theta < 90°$. The Finnie model predicts no wear for a purely normal impact at $\theta = 90°$. The Finnie model has been extended to account for the change of the impact area [20] and shape of impacting particles [21–23]. However, the equations of motion need to be solved numerically as the change of impact area makes them non-linear. One of the most common numerical models for particle impact is the 'rigid-plastic' model, where the crater volume and the time-dependent contact surface are calculated by solving the equations of motion of the particle during the impact [24]. The particle is assumed non-deforming, while the target material deforms plastically (the elastic effects are ignored). The rigid-plastic models do not consider the build-up of material at the edge of the crater and cannot simulate fracture. Some recent works [25–27] used the finite element method in order to simulate the impact. Smoothed-particle hydrodynamics has also been used for this purpose [28,29]: a mesh-free method enables large strains which would distort a computational mesh.

The Archard model studies the wear of two bodies sliding past each other, as in the case of scratch tests where a sharp indenter, which is typically harder than the sample material, is moved tangentially over the surface of interest under a normal load [30]. Scratching is a complex phenomenon, often accompanied by fracture, plastic deformation and material detachment. The Archard model predicts a worn volume proportional to the vertical load and the sliding distance, and inversely proportional to the hardness. A constant of proportionality encompassing many different mechanical/physical effects called a "wear coefficient" is introduced with values varying in a wide range. No dependence on the sliding velocity is assumed. Scratch tests have been modelled and simulated computationally using classical molecular dynamics [31,32], mesh-based continuum mechanical methods [33,34], or meshless continuum methods such as smoothed-particle hydrodynamics [35,36] or the cracking particle method [37,38].

In this paper, a rigid-plastic model is employed in conjunction with DEM. DEM is used here to coarse-grain microscopic interactions and reduce the computational cost in comparison with other methods [39]. We study the plastic wear of a surface in the case of shallow indentation depths and impact craters, smaller than the fracture process zone size [40,41]. Although the rigid-plastic model introduced here certainly presents some limitations, it has several unique advantages:

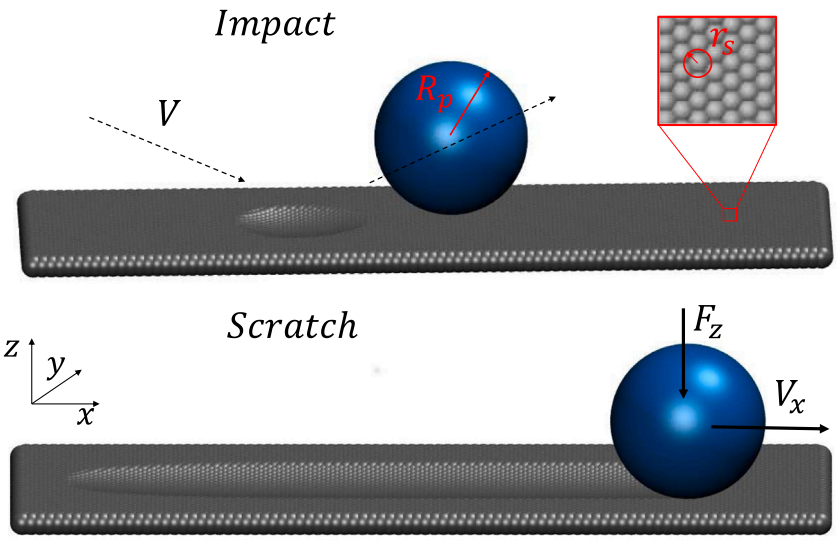

Fig. 1. Setup to simulate the wear of a flat surface induced by impact (top) or scratching (bottom). The surface is made of N small spheres with radii r_s arranged in a hexagonal geometry. A larger spherical particle of radius R_p serves as the projectile or indenter. As a projectile, an initial velocity is assigned to the particle; as an indenter, both a horizontal velocity and a normal load are assigned to the irrotational particle.

- Surface changes caused by wear can be simulated explicitly for any scenario: normal or oblique impact or scratching of a surface.
- Only the surface is simulated. This reduces the total number of particles required in a simulation.
- The implementation of this model is simple and few material parameters are needed to set up the simulation.
- While this paper focuses on the wear of flat surfaces with rigid spheres, the proposed approach may be generalised to surfaces of any closed shape and impacting/indenting particles of any shape.

Section 2 describes the rationale behind the model. It shows how suitable surface displacements are calculated to describe the evolution of a worn surface. Section 3 details the simulations' setup and how the method is practically implemented. In Section 4 the model is compared with experimental results and previous simulation data. It is also demonstrated how the model achieves the energy balance. Finally, the underlying limitations of the approach, future developments and conclusions are presented in Section 5.

2. Model for surface displacements

In this section we introduce a model of wear based on a failure criterion. We describe how suitable displacements dz and $dz_{x,i}$ can be used to modify the surface profile as a consequence of the wear process. A flat surface, with a defined value of the hardness, H, and area, A, is modelled with N small spheres with radii r_s arranged in a hexagonal geometry (Fig. 1). Each sphere represents many microscopic asperities. Since the surface is flat, a constant area per sphere, $a_s = A/N$, may be found. A larger spherical particle, referred to as "particle" in the following, has a radius R_p and serves as the projectile or indenter. As a projectile, an initial velocity is assigned to the particle and its impact with the surface is studied; as an indenter, we assign both a horizontal velocity and a normal load to the irrotational particle and study the "scratching" of the surface. The model is valid for small indentation depths, h, namely $h \ll R_p$ and below a critical depth of cut, so that surface cracks can be neglected [40]. The contact between the particle and each surface sphere is Hertzian, while there is no interaction between the surface spheres. A friction coefficient μ limits the particle–sphere tangential force. We assume the particle's hardness is larger than the hardness of the surface so that the particle's deformation and wear can be neglected. The fines produced during the wear process are also neglected.

During particle–surface interaction, while the pressure, P, on the surface is lower than the material hardness, H, the spheres comprising the surface remain immobile. When the pressure on the surface exceeds H, wear begins and the surface profile is modified. As the particle is in contact with the surface, the surface displacements along the vertical z and lateral x directions can be calculated from the equations of motion of the particle [1]

$$m\ddot{z} = F_z \quad if\ P_z > H \tag{1}$$

$$m\ddot{x} = F_x \quad if\ P_x > \mu_a H \tag{2}$$

where m is the particle's mass, F_z and F_x are the normal and lateral forces on the particle, respectively. By analogy with the Finnie equations [18], the coefficient $\mu_a < 1$ sets the "local" ratio of the tangential to the normal force. The value $H_l = \mu_a H$ is termed the "shear hardness" and is the shear stress needed to wear the surface. We give an operative definition of H_l in Section 3.1 and show that in most practical cases $\mu_a < \mu$. We neglect particle rotation as it can be shown to be small during the impact [18]. According to the original idea of Finnie, $F_z \propto z$, $F_x = \mu_a F_z$ and Eqs. (1) and (2) are always coupled. With these assumptions the equations can be solved and the swept volume estimated [18].

However, forces and velocities are known at all times in a DEM simulation which makes these assumptions unnecessary. The forces F_x and F_z can be considered constant within the very small time increment dt adopted in DEM. Additionally, the conditions $P_z > H$ and $P_x > \mu_a H$ can hold separately and Eqs. (1) and (2) are not coupled. When Eqs. (1) and (2) are integrated in the time interval $[t, t+dt]$, the variations $dx(t+dt)$ and $dz(t+dt)$ give

$$\begin{aligned} dz(t+dt) &= \frac{1}{2m} F_z(t)(dt)^2 + V_z(t)dt \\ dx(t+dt) &= \frac{1}{2m} F_x(t)(dt)^2 + V_x(t)dt \end{aligned} \tag{3}$$

where $V_x(t)$ and $V_z(t)$ are the components of the particle's velocity at time t. The $1/2$ factor in Eq. (3) is due to the velocity-Verlet integration scheme commonly used in DEM. Of course the equations of motion can be written in three dimensions, but for simplicity here we assume the lateral displacement during impact or scratching takes place solely in the x direction. Indicating with k either of the x or z components and considering that $F_k/m\ dt = dV_k$ (with dt small), the second-order term in Eq. (3) contributes to the displacement as $1/2\ dV_k\ dt$ and can effectively be neglected (as far as $V_k(t) \neq 0$) to give

$$dz(t+dt) \approx V_z(t)dt$$

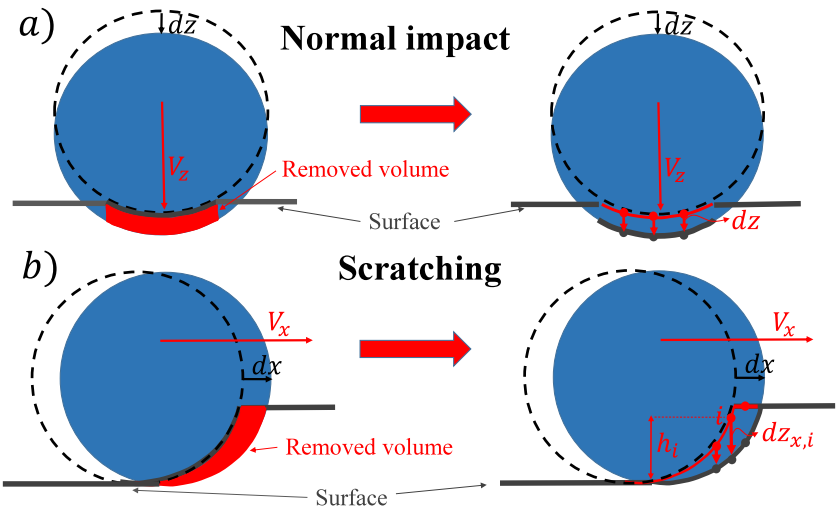

Fig. 2. (a) The surface change in the case of normal impact is obtained by displacing the "flowing" spheres an amount dz in the normal direction. (b) Surface change in the case of pure scratching. When the indenter translates a distance of $dx = V_x dt$ in the x direction, the surface profile is obtained by translating the spheres incrementally by $dz_{x,i}$ in the vertical direction.

$$dx(t+dt) \approx V_x(t)dt \tag{4}$$

When wear occurs, the surface profile is modified. We use dx and dz to calculate the corresponding displacements of the surface spheres to obtain the worn profile. A surface sphere with index i enters the "flow" regime when the force $F_{z,i} > a_i H$ ($P_z = F_{z,i}/a_i$) and/or $F_{x,i} > a_i H_l$ ($P_x = F_{x,i}/a_i$). The area $a_i = a_s \frac{r}{r-h_i}$ is an effective area per sphere which accounts for the increase of area due to surface indentation, with h_i denoting the indentation depth of sphere i (see Appendix A for more details). Here, $r = r_s + R_p$ represents the effective radius: the sum of the small sphere and particle radii.

In the case of a pure, normal impact, $V_x = 0$, $V_z \neq 0$ and the wear volume $dW_V \sim \sum_{i=1}^{n_f} dz\ a_s$, where n_f is the number of spheres in the flow regime. Therefore, the surface profile after a time dt is obtained by displacing the n_f "flowing" spheres an amount dz in the normal direction, as shown in Fig. 2a.

The case of a scratch ($V_x \neq 0$, $V_z = 0$) is more complex. We will not displace the spheres laterally to keep the discretisation as uniform as possible. Instead we calculate the removed volume and displace the spheres in the normal direction to model the crater of impact, as shown in Fig. 2b.

When the indenter translates a distance of $dx = V_x\ dt$ in the x direction and the lateral pressure $P_x > \mu_a H$ on n_f spheres, a volume must be removed (red region in Fig. 2b). The wear volume can be calculated as $dW_V \sim \sum_{i=1}^{n_f} a_s\ dz_{x,i}$ where

$$dz_{x,i} \sim h_i - r + \sqrt{(r-h_i)^2 + 2\sqrt{2rh_i - h_i^2}dx} \tag{5}$$

is the vertical distance between the old position of sphere i and the surface of the translated indenter, with h_i the sphere-dependent indentation depth and dx small. The derivation of $dz_{x,i}$ is shown in Appendix B. Eq. (5) shows that $dz_{x,i} = 0$ when $dx = 0$, while $dz_{x,i} \to 0$ when $h_i \to 0$, as expected. Therefore, the total worn surface after a scratch can be obtained by translating the spheres incrementally by $dz_{x,i}$ in the vertical direction.

The wear volume at time t, $W_V(t)$, is easily estimated from the relation

$$W_V(t) \approx \sum_{i=1}^{N}(z_0 - z_i(t))a_s = (N z_0 - \sum_{i=1}^{N} z_i(t))a_s \tag{6}$$

where z_0 is the vertical coordinate of the spheres at $t = 0$ when the surface is flat.

3. Setup of DEM simulations

The DEM code used was the open-source, MPI-parallelised code LAMMPS [42] and the granular package. The surface, a strip of length $L = 9.35$ cm and width $S = 1.68$ cm, is made of $N = 5012$ spheres with radii $r_s = 0.25$ mm arranged in a hexagonal geometry and not interacting with each other. In the case of a flat surface, an area $a_s = L \cdot S/N \sim 0.31$ mm^2 corresponds to each sphere. A surface hardness, $H = 1.7$ GPa, is considered (unless otherwise specified) by assigning to the surface sphere with index i a failure force $F_{z,i} = a_i H$, where a_i is the area corresponding to the sphere i. During the simulation, we do not compute the pressure but the force on the surface spheres: a change of a_i (e.g., due to indentation as described in Appendix A) is reflected in a change of the failure force $F_{z,i}$. The particle used as a projectile has a radius $R_p = 3$ mm, while the indenter has a radius $R_p = 1$ cm. The number of spheres and their radii have been chosen carefully to reduce artificial oscillations during the sliding caused by discretisation of the surface. With the current arrangement the amplitude of such oscillations is $\sim 1\,\mu$m: much smaller than the indentation depth, h, and the radius of the particle R_p. The contact between the particle and each surface sphere is Hertzian with Young's modulus $E = 200$ GPa and Poisson's ratio $\nu = 0.3$ [42,43]. These values describe the elastic properties of the surface spheres, as the particle is assumed rigid and undeformable. The magnitude of the tangential force is limited to a fraction of the magnitude of the normal force at a contact using a fixed friction coefficient, set here to $\mu = 0.5$ although the values reported in literature show wide variability [9]. The implementation of the wear model is done in LAMMPS directly through the input script. Vertical, i_V, and lateral, i_L, "flow" indexes are assigned to each surface sphere i as follows:

$$i_V = \begin{cases} 1, & \text{if } F_{z,i} > a_i H \quad (flow) \\ 0, & \text{otherwise.} \end{cases} \tag{7}$$

and

$$i_L = \begin{cases} 1, & \text{if } F_{x,i} > a_i H_l \quad (flow) \\ 0, & \text{otherwise.} \end{cases} \tag{8}$$

where $H_l = \mu_a H$ is the "shear hardness", a lateral pressure to initiate the wear process (see Section 3.1). Wear is simulated by moving the spheres along the z direction. The vertical displacements of spheres are calculated on each time-step through the relations $dz(t+dt) = V_z(t)dt$ and Eq. (5), but only the ones with $i_V = 1$ and/or $i_L = 1$ are effectively displaced. The overall displacement of the surface sphere i is

$$\Delta z_i(t) = dz\ i_V + dz_{x,i}\ i_L \tag{9}$$

The surface spheres are displaced through the *fix move* command in LAMMPS. A sphere velocity $\Delta z_i(t)/dt$ is assigned to sphere i, while the displacement variables are specified as NULL. The positions of the spheres are then time-integrated using that velocity.

Eqs. (7)–(9) ensure that during wear the vertical and/or lateral pressures remain fixed at H and/or H_l, respectively. "Flowing" spheres satisfy conditions (7) and/or (8) which contribute respectively to the vertical, $F_{z,V}$, and lateral, $F_{x,L}$, forces on the particle as:

$$F_{z,V} = \sum_{i=1}^{N} H\ a_i\ i_V \tag{10}$$

$$F_{x,L} = \sum_{i=1}^{N} H_l\ a_i\ i_L \tag{11}$$

The meaning of Eq. (10) is straightforward in the case of a shallow indentation of the surface. In that case $a_i \sim a_s$, the surface spheres are displaced vertically at the same velocity, V_z, as the particle, and $F_{z,V} \sim H a_s \sum_{i=1}^{N} i_V$, where $H a_s$ represents the maximum possible contribution of the sphere to the vertical force. We point out that a flowing sphere can contribute to both the vertical and lateral component of the force when only one of the conditions (7) or (8) is true. For instance, when condition (8) is true for the sphere i (scratching), the lateral force is fixed at $F_{x,i} = a_i H_l$, while the vertical component of force is the projection of the particle–sphere Hertzian force on the z axis. As the spheres are not interacting with each other, the described approach can only simulate plastic deformations and not fracture or the build-up of material at the leading edge of the scratching/impacting particle.

We use this approach both for impact and scratching simulations. In the first case, an initial velocity V is given to the impacting particle, with components V_x and V_z such that $V = \sqrt{V_x^2 + V_z^2}$. For simplicity, we assume the component of velocity parallel to the flat surface lies on the x-axis.

In the second case (scratching simulations), the surface is first indented by displacing the particle (the indenter) at a constant velocity of $V_z = -0.1\,\mathrm{cm\,s^{-1}}$. The positions of the particle and surface spheres are saved at different stages of the indentation process along with the corresponding normal force, F_z, on the indenting particle. Afterwards, starting from the saved positions and keeping the corresponding F_z fixed, the indenter is displaced at a constant velocity $V_x = 20\,\mathrm{cm\,s^{-1}}$. These scratching simulations are performed by disabling the rotational degrees of freedom of the indenter. These constant-velocity simulations have been run for 0.4 s. This time interval is long enough to ensure that a stationary state is reached and the vertical position of the indenter remains constant.

3.1. The shear hardness H_l

Here we give an operative definition of the shear hardness. Our everyday-life experience shows that a hard tip can scratch a softer surface even without an initial indentation. More specifically, we will address the case where $P_z < H$, so no indentation or permanent impression is left on the surface when only a normal force is applied to the tip. However, when the tip moves laterally and P_z is large enough, a wear track is left on the surface. Clearly, the concept of dynamic "scratch hardness", $H_s = F_z/A_z$ (with A_z the area of contact orthogonal to the vertical load), cannot be used to characterise the resistance to scratching as it does not account for the friction force F_x at the interface [44]. The concept of "ploughing hardness", $H_p = F_x/A_x$, is difficult to use as the lateral area A_x (the portion of the contact area orthogonal to the scratching direction) can be negligibly small and difficult to quantify [45], while F_x is finite.

The friction force, $F_x = \mu F_z$, is related to the normal force, F_z, through the friction coefficient, μ. The situation above (scratching with no indentation) is described by the conditions

$$F_x > \mu_a A_z H \tag{12}$$

$$F_z < A_z H \tag{13}$$

As $F_x = \mu F_z$ is the maximum lateral force, from Eq. (12) $\mu F_z > \mu_a A_z H$ and $F_z > \frac{\mu_a}{\mu} A_z H$. This last condition is satisfied together with Eq. (13) only if $\mu_a < \mu$.

A simple simulation can be used to show that μ_a sets the resistance to scratching, and how the shear hardness H_l can be estimated by calculating the quantity $H_l = \frac{dF_x}{dA_z}$ as soon as the scratch starts. Assume $\mu = 0.5$ and $\mu_a = 0.25$. We first move the indenter at a velocity $V_z = -0.001\,\mathrm{m\,s^{-1}}$ in the z direction and save the position and normal force F_z on the indenter. Afterwards, starting from the saved positions and corresponding values of F_z, we move the indenter at a constant velocity $V_x = 0.2\,\mathrm{m\,s^{-1}}$. When F_z is small, no wear is visible on the surface. Wear starts when the load is above the threshold $F_z \sim 1000\,\mathrm{N}$, as shown in Fig. 3a where we report the wear volume per distance travelled as a function of F_z (raw data sets of figures can be found at [46]). At the threshold and four values of F_z above the threshold, we measure the lateral force, F_x, and the area normal to the load, A_z. The area A_z has been approximated with the contact area, calculating the number of surface spheres in contact with the indenter. The shear hardness $H_l = \frac{dF_x}{dA_z}$ is the slope of the line in Fig. 3b. The estimation gives $H_l \sim 0.37\,\mathrm{GPa}$. Note that $H_l \sim \mu_a H$ as expected. The discrepancy in the estimation of H_l is due to the overestimation of the area A_z, as the spheres at the boundary of the indentation and at the trailing edge of the indenter do not contribute to the lateral force F_x.

4. Validation of the model

In this section we compare the wear volume obtained with this model to some theoretical predictions and numerical results. We use this model for both impact and scratching simulations.

4.1. Normal impact

Here we study the case of a normal impact ($V_x = 0$), when the velocity V_z of the particle is large enough for the surface spheres to flow. As the particle is a sphere, the indented area $A_c = 2\pi R_p h$ is a spherical cap where R_p is the radius and h the indentation depth. We assume that the force exerted by the surface on the particle is

$$F_{\mathrm{surf}} = -2\pi R_p h H, \tag{14}$$

with H the hardness. We neglect the contribution to the force from the peripheral surface spheres: those in contact with the indenter but not yet in the flow regime. In this simplified scenario, the equation of motion of the particle in contact with the surface is

$$m\ddot{h} = -2\pi\ R_p\ h\ H \tag{15}$$

Eq. (15) is easily solved with the boundary conditions $h(0) = 0$, $\dot{h}(0) = V_z$ to give $h(t) = \frac{V_z}{\alpha} sin(\alpha t)$, with $\alpha = \sqrt{\frac{2\pi\ R_p\ H}{m}}$.

The indentation depth h has a maximum at some time t_m where the vertical velocity becomes 0, i.e., $\dot{h}(t_m) = V_z cos(\alpha t) = 0$ and $t_m = \frac{\pi}{2\alpha}$ (here we ignore the effect of elastic deformation). Therefore $h_{max} = h(t_m) = \frac{V_z}{\alpha} sin(\alpha t_m) = \frac{V_z}{\alpha}$. Considering that the volume of the spherical cap is $V_{cap} = \pi h^2 (R_p - \frac{h}{3})$, the wear volume for a normal impact can be estimated as

$$W_V \sim \pi h_{max}^2 R_p = (V_z)^2 \frac{m}{2H} \tag{16}$$

where we have assumed $h \ll R_p$. A similar relation between the kinetic energy and the wear volume was obtained by Finnie [18] and other groups [16,47].

The wear volume, W_V, caused by a particle of radius $R_p = 1\,\mathrm{cm}$ and density $\rho = 8\,\mathrm{g\,cm^{-3}}$ impacting the surface vertically is shown in Fig. 4. Fig. 4a shows W_V as a function of the hardness, H, for a fixed vertical velocity $V_z = 45\,\mathrm{m\,s^{-1}}$, while in Fig. 4b W_V is shown as a function of the velocity for a fixed hardness $H = 1.7\,\mathrm{GPa}$. There is a fair agreement between the theoretical estimation and the simulation results.

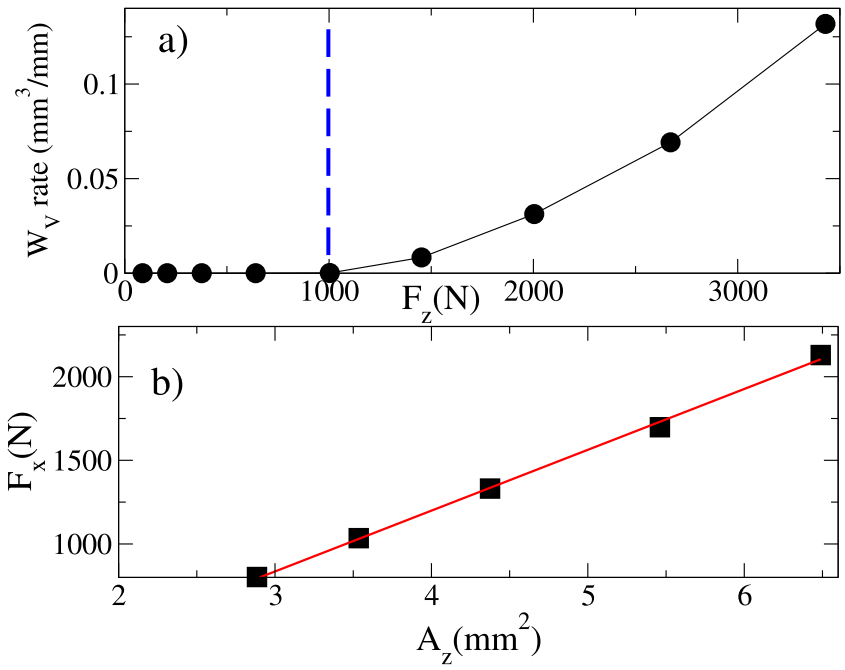

Fig. 3. (a) Wear volume per distance travelled as a function of vertical load F_z. Wear starts above a threshold (vertical dashed line). (b) Lateral force F_x as a function of the area normal to the load A_z, computed at the threshold and above. The shear hardness, H_l, is the slope of the red line.

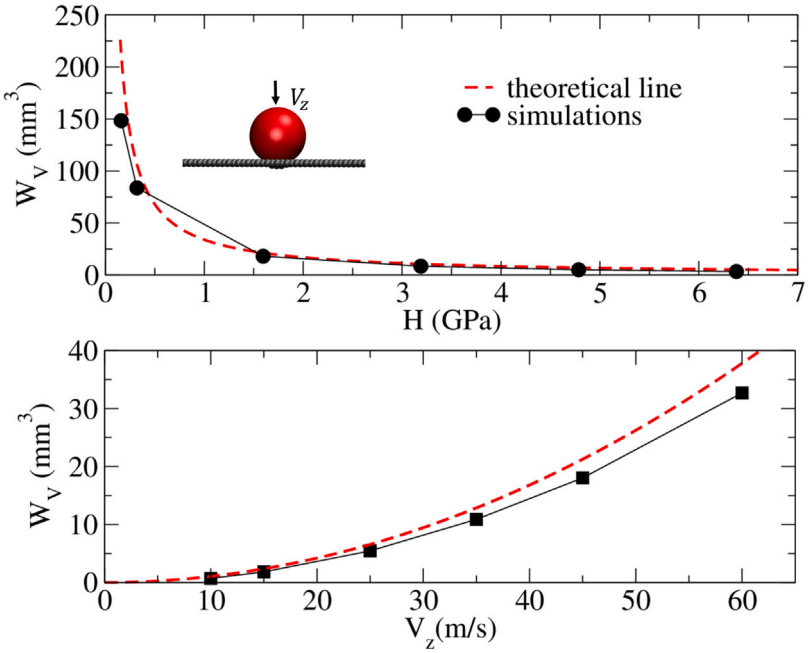

Fig. 4. (top) Wear volume as a function of the hardness, H, for a vertical velocity $V_z = 45\,\mathrm{m\,s^{-1}}$. (bottom) Wear volume as a function of the velocity, V_z, for a hardness $H = 1.7\,\mathrm{GPa}$.

4.2. Oblique impact

In this section we show how the wear volume changes for the case of an oblique impact. We simulate the impact of a spherical particle with a density of $2.5\,\mathrm{g\,cm^{-3}}$ and radius $R_p = 3\,\mathrm{mm}$ on a hard steel surface with hardness $H = 6.6\,\mathrm{GPa}$. In this set of simulations, the hardness of the surface has been changed to provide a better comparison with available experimental data [48–50]. Wear appears only above a threshold velocity [19]. Above the threshold velocity, we plot the wear volume as a function of the impact angle θ. The results are reported in Fig. 5a for three velocities, $V = 30, 35, 40\,\mathrm{m\,s^{-1}}$. The wear volume grows with the velocity and has a peak between 0 and 90° as reported in literature [1,18,19,47–50]. As a "normal" term has been included in the modelling (see Fig. 2a), the simulations can capture wear even at 90°.

Fig. 5b shows the contributions of the normal and scratch components to the wear volume in the case of $V = 35\,\mathrm{m\,s^{-1}}$. As expected, the normal component (often referred to as the "deformation" component) is the main contributor to erosive wear at angles close to 90°. As the angle reduces ($\theta \sim 75°$), the normal component declines and the scratch component takes over.

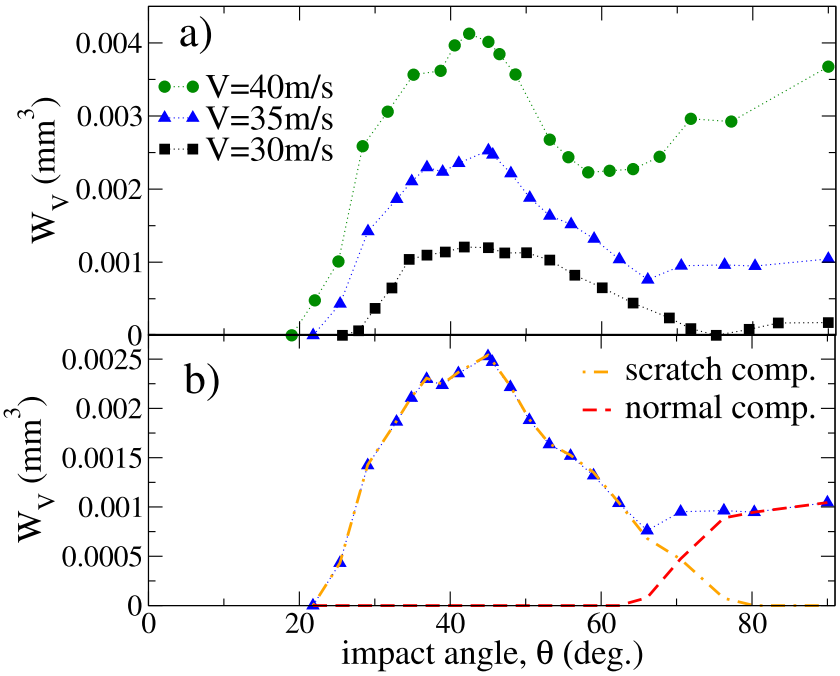

Fig. 5. (a) Wear volume as a function of the impact angle θ for three velocities, V = 30, 35, 40 m s^{-1}. (b) Contributions of the normal and scratch components to the wear volume for V = 35 m s^{-1}.

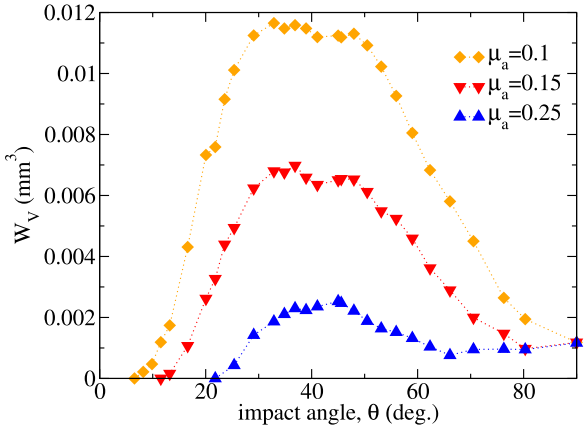

Fig. 6. Wear volume as a function of the impact angle θ for μ_a = 0.1, 0.15, 0.25 and V = 35 m s^{-1}.

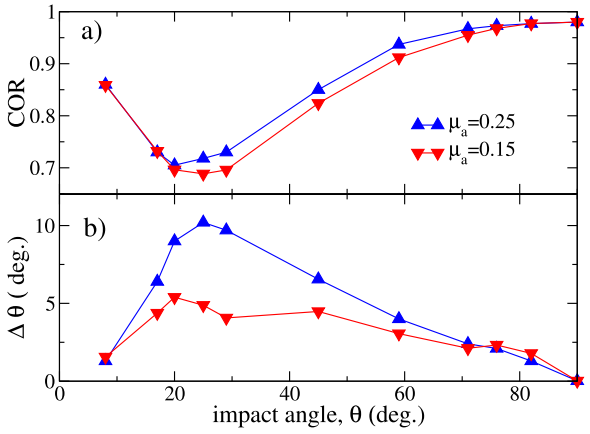

Fig. 7. (a) Coefficient of restitution COR as a function of the impact angle θ. (b) Angle of deviation $\Delta\theta$ as a function of θ. Here μ_a = 0.15, 0.25 and V = 35 m s^{-1}.

The previous results have been obtained with a fixed value of μ_a = 0.25. Fig. 6 compares the wear volume at μ_a = 0.1, 0.15, 0.25 as a function of the angle at V = 35 m s^{-1}. As μ_a sets the lateral hardness to initiate scratching, by reducing μ_a the scratch component becomes relevant at larger angles, contributing to larger wear volumes.

The impact can modify not just the surface but also affect the particle's motion, as part of the initial kinetic energy is lost during the impact (see Section 4.4). To study how the particle's motion changes after the impact, we define a coefficient of restitution, COR, and an angle of deviation, $\Delta\theta$, as

$$COR = \frac{V_r}{V} \tag{17}$$

$$\Delta\theta = \theta_r - \theta \tag{18}$$

where V_r and θ_r are the rebound velocity and angle, respectively. Both the COR and $\Delta\theta$ show a strong dependence on the angle of impact θ as reported in Fig. 7. Close to $\theta \sim 90°$ the $COR \sim 1$ and $\Delta\theta \sim 0$ as a negligible part of the translational kinetic energy is dissipated. However, further from $\theta \sim 90°$, the COR decreases to a minimum at $\theta \sim 25°$ while $\Delta\theta$ reaches a maximum at about the same angle. The maximum of the wear volume is at a different value, $\theta \sim 45°$ (Fig. 6). While the minimum of the COR corresponds to a maximum dissipation of the initial kinetic energy, the maximum of the wear volume corresponds to a maximum of the sole wear component of the dissipation (see Section 4.4). As shown in Fig. 7, a lower value of μ_a = 0.15 reduces both the restitution coefficient and $\Delta\theta$, recalling that μ_a is a simulation parameter that can be obtained through the experimental procedure explained in Section 3.1.

4.3. Scratching

The surface is first indented by moving the indenter at a constant velocity V_z = 1 mm s^{-1} in the z direction. The force–displacement curve is reported in Fig. 8a. At small values of the indenter's displacement, z, the force F_z = 0 as there is no contact. Post-contact and for F_z < 3 kN, the surface responds elastically and no permanent impression is

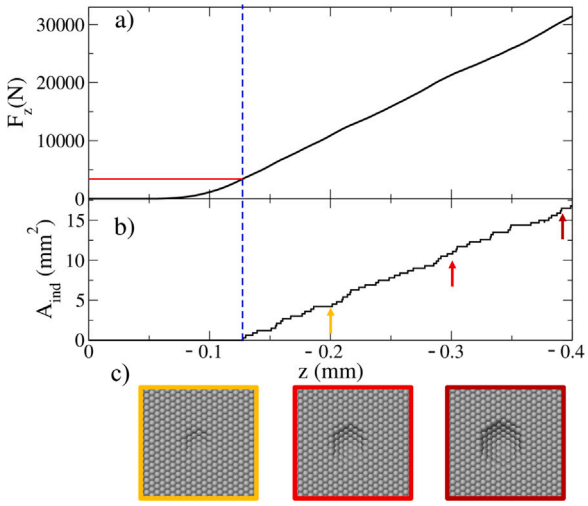

Fig. 8. (a) Vertical force F_z as a function of the displacement z. (b) Evolution of the indented area as a function of z. (c) Snapshots of the indented areas for three values of z corresponding to the arrows in panel (b).

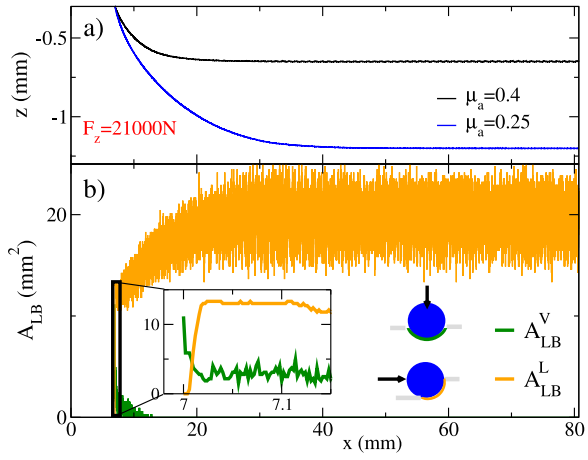

Fig. 9. (a) Vertical coordinate, z, of the indenter as a function of the distance travelled, x, at a load $F_z = 21\,\text{kN}$ and for $\mu_a = 0.25$, 0.4. (b) Evolution of the vertical, A^V_{LB}, and lateral, A^L_{LB}, load-bearing areas as a function of x during the transition from indentation to scratching. Here $\mu_a = 0.25$.

left on the surface. However above $F_z \sim 3\,\text{kN}$, the normal pressure $P_z > H$ and the surface spheres start to flow; as a consequence the surface is permanently deformed. In fact, a clear impression is left on the surface when the indenter is removed. The evolution of the indented area, $A_{ind}(z) = \sum_{i=1}^{N} a_i(z) \cdot i_V$, as a function of z is shown in Fig. 8b, with i_V the flow index defined in Eq. (7). Snapshots of the indented areas for three values of z (coloured arrows) are shown in Fig. 8c.

Starting from the positions and forces saved during the indentation, the indenter is moved at a constant velocity $V_x = 20\,\text{cm}\,\text{s}^{-1}$ while keeping the corresponding F_z fixed and without permitting rotation of the indenter.

The evolution of the vertical z coordinate of the indenter at a load $F_z = 21\,\text{kN}$ is shown in Fig. 9a for the indicated values of μ_a. During the quasi-static indentation, the normal load is counterbalanced by the contact force from the indented area, A_{ind}, which constitutes the load-bearing area, A_{LB}. We have studied the evolution of A_{LB} from indentation to scratching, separating the contributions of the vertical, A^V_{LB}, and lateral, A^L_{LB}, load-bearing areas [32], where:

$$A^V_{LB} = \sum_{i=1}^{N} a_i i_V \tag{19}$$

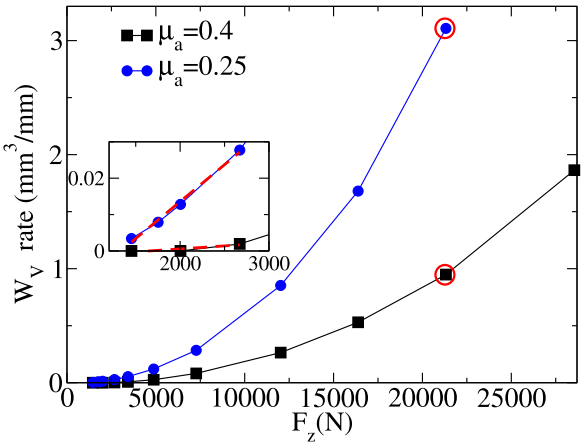

Fig. 10. Wear volume per distance travelled as a function of the normal load F_z. A linear relationship between W_V rate and F_z is observed only at small values of F_z (inset). Snapshots of the scratching simulations corresponding to the red circles are reported in Fig. 11.

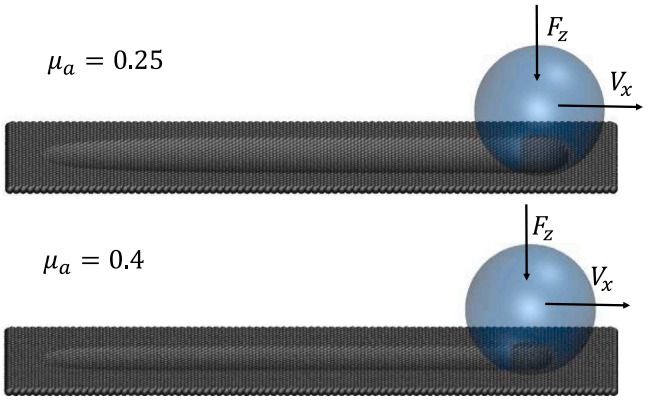

Fig. 11. Snapshots of two scratching simulations for a soft (top) and hard (bottom) surface corresponding to the red circles in Fig. 10. μ_a sets the resistance to surface scratching.

$$A^L_{LB} = \sum_{i=1}^{N} a_i i_L \tag{20}$$

Clearly, $A^L_{LB} = 0$ during the indentation. However, when the indenter is displaced laterally, its back side moves away from the indented area and A^V_{LB} is immediately reduced. This is shown in Fig. 9b where A^V_{LB} decreases sharply from its initial value $\sim 12\,\text{mm}^2$. As a result the indenter penetrates deeper into the surface (see Fig. 9a) until a new equilibrium is found when the contact forces from the new load-bearing area A^L_{LB} balance the normal load. Therefore, the resistance to the lateral motion comes from the force to displace the spheres ahead of the indenter (see Eq. (11)). This force pushes against the leading side of the indenter which generates an upward component of force.

Fig. 10 shows the wear volume per distance travelled, as a function of the normal load. Contrary to Archard's law, the relationship in non-linear. However, the behaviour is in qualitative agreement with numerous experimental data and simulations [51–54]. As displayed in the inset of Fig. 10, a linear relation is only maintained within a certain range of applied loads [55]. The two curves in Fig. 9a correspond to $\mu_a = 0.25$ and 0.4 and demonstrate that μ_a sets the resistance of the surface to scratching. A high value of μ_a makes the scratch more shallow as shown in the snapshots in Fig. 11.

Unlike in many experiments [45,56,57] and simulations [58,59], the proposed approach does not account for the build-up of material at the leading edge of the indenter. Third body effects and the wear

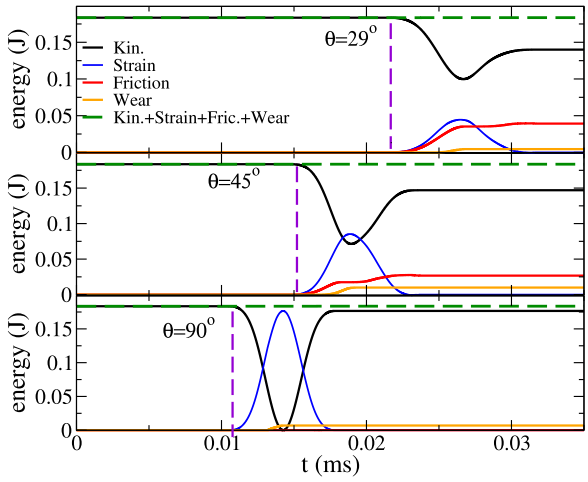

Fig. 12. Energy terms (kinetic, strain, dissipation by friction and wear) as a function of time for the impact of a spherical particle at indicated angles θ at velocity $V = 35\,\mathrm{m\,s^{-1}}$. The horizontal green dashed line is the sum of all terms. The vertical dashed line indicates the time of impact.

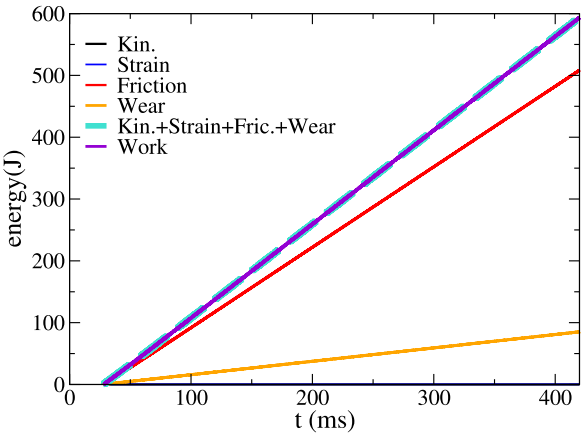

Fig. 13. Energy terms (kinetic, strain, dissipation by friction and wear) as a function of time for a spherical particle scratching a surface at $V_x = 20\,\mathrm{cm\,s^{-1}}$. The sum of all energy terms exactly matches the work done by the external force to keep the indenter moving at constant velocity.

material are not accounted for; this is of course a limitation of the model that we discuss more in detail in Section 5.

4.4. Energy balance and dissipation

Wear introduces a new means of energy dissipation into the system, along with the frictional dissipation (all other sources of dissipation have been disabled). In this section we show that, taking into account the "wear dissipation", the system achieves an energy balance. During the simulation, we monitor the kinetic and strain energy, along with the dissipative frictional and wear energy terms. The kinetic energy includes both translational and rotational terms, while the strain energy is the elastic energy at the Hertzian contacts. The calculation of strain energy is divided into normal and tangential components, the latter requiring incremental calculation [60]. The energy dissipated in frictional sliding is calculated incrementally: when a slip criterion is satisfied, the average tangential force at the single contact is multiplied by the slip displacement. The total frictional dissipation is found by summation over all contacts [60].

The energy dissipated by wear at surface sphere i during time-step k is the work done by the vertical force $F_{i,z}$ to displace the sphere i:

$$\delta E_i^k = F_{i,z}(dz\, i_V + dz_{x,i}\, i_L) \tag{21}$$

where the indexes i_V and i_L have been defined in Section 3 and $dz_{x,i}$ is given in Eq. (5). The total wear dissipation by time-step k is found by summation over all N spheres:

$$E_i^k = E_i^{k-1} + \sum_{i=1}^{N} \delta E_i^k \tag{22}$$

This summation over spheres relies on the fact that each surface sphere can have a maximum of one contact for this simulation configuration. Fig. 12 shows all energy terms as a function of time for the case of the impact of a spherical particle at different angles, $\theta = 29°, 45°, 90°$.

At $t = 0$, the particle is given an initial velocity and the corresponding kinetic energy (black curve) is not conserved. After impact (vertical lines in the panels), part of the kinetic energy is converted to elastic strain energy (blue line) which is recovered when the particle leaves the surface. Part of the original kinetic energy is dissipated in friction and wear. However, the sum of the four energy terms (horizontal green dashed lines) shows that the energy balance is achieved.

We have also verified the energy balance is achieved in the case of scratching. In this case, energy is continuously added to the system to move the indenter at a constant velocity V_x. This energy can be calculated from the work done by the external force, F_{ext}, on the indenter:

$$Work(t) = \int_0^t F_{ext}(t) V_x dt \tag{23}$$

As shown in Fig. 13 the sum of the four energy terms exactly matches the work of the external force, with the main contributions coming from the wear and frictional dissipation terms.

5. Conclusions and future developments

This article introduces a failure model capable of describing wear in both impact and scratching scenarios by explicitly simulating the evolution of a surface using the discrete element method. The model is efficient as it requires relatively few particles to simulate the surface evolution (not the bulk) and parsimonious in terms of the number of parameters used (material characteristics enter through the hardness and friction coefficient). The simulations show good qualitative agreement with experimental data and previous numerical results. For impact cases, the wear volume increases with the incident velocity and has a peak between 0 and 90°. For scratching cases, the wear volume is proportional to the normal load in a limited range of loads, in accordance with Archard's law, and transitions to a non-linear behaviour at higher loads. When all sources of energy dissipation have been considered, the model achieves the energy balance.

All numerical models have some limitations. The proposed approach cannot describe the long-range elastic response of the worn surface: a limitation shared with other models such as Archard and Finnie which do not account for the elasticity of the surface. Furthermore, the current model does not account for the build-up of material at the leading edge of the indenter, as the spheres modelling the surface are enforced to move only in the normal direction. Neglecting the build-up of material has the effect of reducing the lateral area and the resistance to scratching.

This article focuses on the wear of flat surfaces due to impact/indentation with rigid spheres. This is not due to an inherent limitation of the simulation method; future research will extend this study to the wear of surfaces of any arbitrary closed shape and impacting/indenting particles of any shape. This will include the application of this approach to model the wear between many bodies, e.g., a granular system. The displacement of a surface point is always in the vertical direction for the flat surfaces considered in this paper; in general the displacement vector will be oriented normal to any irregular, closed

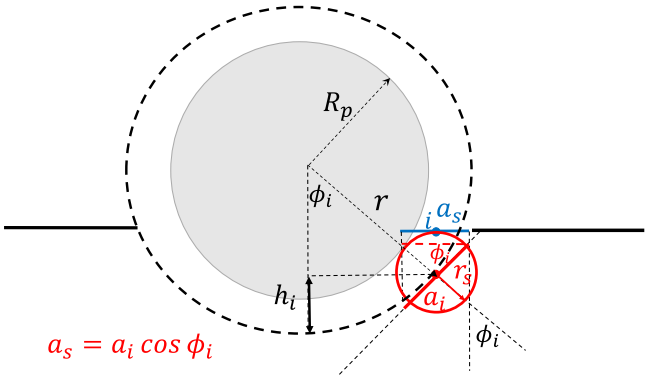

Fig. 14. Sketch of the area transformation $a_s \rightarrow a_i$ due to the indentation. When the spherical particle with radius R_p touches the small sphere with radius r_s, a_i is calculated considering the effective radius $r = R_p + r_s$ of the equivalent sphere and a point-like particle at the centre of the small sphere.

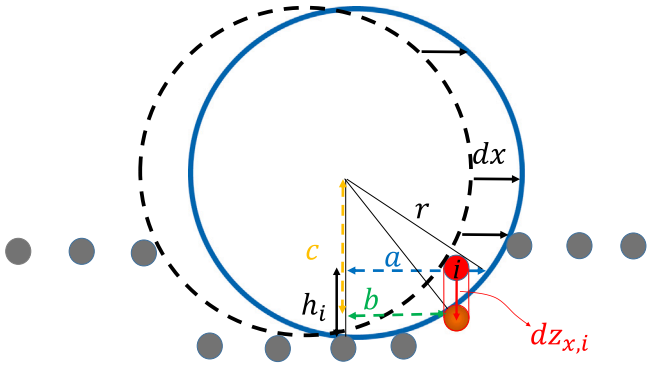

Fig. 15. When the indenter moves a distance dx, a volume must be removed which corresponds to the volume of a cylinder with cross-sectional area a_s and height $dz_{x,i}$ (red particle i).

surface. Additionally, the area (or mesh) elements associated with the points describing the surface are, in general, different. For this reason the generalisation to irregular surfaces requires the calculation of the normal and local area associated with each surface point. Impacting or indenting particles of any shape can be implemented using the conventional multi-sphere clump approach in DEM. In this case, the calculation of surface displacements dz and $dz_{x,i}$ requires the velocity and position of the particular sphere of the clump in contact with the surface.

CRediT authorship contribution statement

R. Capozza: Conceptualization, Methodology, Writing – original draft, Writing – review & editing, Investigation, Visualization. **K.J. Hanley:** Conceptualization, Methodology, Writing – original draft, Writing – review & editing, Funding acquisition, Project administration.

Declaration of competing interest

The authors declare that they have no known competing financial interests or personal relationships that could have appeared to influence the work reported in this paper.

Data availability

There is a link in the manuscript where data can be downloaded

Acknowledgements

This research was funded by the UK Engineering and Physical Sciences Research Council (EPSRC) grant EP/R005877/1. For the purpose of open access, the author has applied a Creative Commons Attribution (CC BY) licence to any Author Accepted Manuscript version arising from this submission. We thank Kevin Stratford (EPCC) and James Young (University of Edinburgh) for their helpful comments during development of this wear model.

Appendix A. Calculation of the effective area a_i

While the surface remains flat, a constant area $a_s = A/N$ is associated with each surface sphere, with A representing the area of the flat surface and N the number of spheres comprising the surface. However, this area increases after indentation/impact as the surface becomes curved at the impact region, while N remains the same.

When surface sphere i is displaced, the new area a_i can be calculated considering that the projection of a_i on the plane of the flat surface remains a_s. The calculation simplifies considerably by considering an effective sphere with radius $r = R_p + r_s$ and a point-like particle located at the centre of the small sphere (see Fig. 14). The two spheres touch when the effective sphere touches the centre of the small sphere. Fig. 14 shows how the area a_s corresponding to i (blue segment) transforms into the area a_i (red segment) as an effect of the indentation. Clearly $a_i = \frac{a_s}{\cos\phi_i}$ where ϕ_i is the angle between the vertical axes passing through the centre of the particle and the line joining the centre and the sphere i. As $\cos\phi_i = \frac{r-h_i}{r}$, with h_i representing the sphere indentation depth,

$$a_i = a_s \frac{r}{r - h_i} \tag{A.1}$$

Appendix B. Calculation of $dz_{x,i}$

During scratching, surface spheres are displaced in the normal direction (not in the lateral direction) to maintain a discretisation that is as uniform as possible. When the indenter moves a distance dx, a volume $dW_{V,i} = a_s\, dz_{x,i}$ must be removed from the surface. It corresponds to the volume of a cylinder with cross-sectional area a_s and height $dz_{x,i}$, referring to the red particle i indicated in Fig. 15.

The surface change is taken into account by displacing the surface sphere by a distance $dz_{x,i}$ in the vertical direction. From simple geometric considerations, the following quantities can easily be calculated:

$$a = \sqrt{r^2 - (r - h_i)^2} = \sqrt{2rh_i - h_i^2} \tag{B.1}$$

$$b = a - dx \tag{B.2}$$

$$c = \sqrt{r^2 - b^2} = \sqrt{r^2 - \left(\sqrt{2rh_i - h_i^2} - dx\right)^2} \tag{B.3}$$

Therefore,

$$dz_{x,i} = c - (r - h_i) \sim h_i - r + \sqrt{(r - h_i)^2 + 2\sqrt{2rh_i - h_i^2}\,dx}$$

where $r = r_s + R_p$ is the effective radius (the sum of the small sphere and particle radii) and h_i is the indentation depth calculated with respect to the position of small sphere i. The term dx^2 has been neglected as the x displacement is infinitesimal. It is easy to verify that $dz_{x,i} = 0$ when $dx = 0$ (no lateral displacement), while $dz_{x,i} \rightarrow 0$ when the sphere indentation depth $h_i \rightarrow 0$, as expected.

We have calculated here the displacement $dz_{x,i}$ taking advantage of the spherical geometry of the particle scratching the surface; however, the same scheme is easily generalised to sphere clumps of any shape, or irregularly shaped particles with a well-defined local radius of curvature.

References

[1] I. Finnie, Erosion of surface by solid particles, Wear 3 (1960) 87–103.
[2] F. Wu, D. Wu, Attrition resistances and mechanisms of three types of FCC catalysts, Powder Technol. 305 (2017) 289–296.
[3] V.A. Golovanevskiy, R.A. Bearman, Gouging abrasion test for rock abrasiveness testing, Int. J. Miner. Process. 85 (2008) 111–120.
[4] S.C. Tung, Y. Huang, Modeling of abrasive wear in a piston ring and engine cylinder bore system, Tribol. T. 47 (1) (2004) 17–22.
[5] D. Forsström, P. Jonsén, Calibration and validation of a large scale abrasive wear model by coupling DEM-fem: Local failure prediction from abrasive wear of tipper bodies during unloading of granular material, Eng. Fail. Anal. 66 (2016) 274–283.
[6] Y. Li, H. Zhang, Z. Lin, Z. He, J. Xiang, X. Su, Relationship between wear formation and large-particle motion in a pipe bend, Royal S. Open Sci. 6 (2019) 181254.
[7] J. de Bono, H. Li, G. McDowell, A new abrasive wear model for railway ballast, Soils Found. 60 (2020) 714–721.
[8] I. Deiros Quintanilla, G. Combe, F. Emeriault, C. Voivret, J. Ferellec, Xray CT analysis of the evolution of ballast grain morphology along a MicroDeval test: key role of the asperity scale, Granul. Matter 21 (2019) 30–1–30–12.
[9] C.P.Y. Wong, M.R. Coop, Development of inter-particle friction in a railway ballast, Géotech. Lett. 10 (2020) 535–541.
[10] V. Nardelli, M.R. Coop, J.E. Andrade, F. Paccagnella, An experimental investigation of the micromechanics of Eglin sand, Powder Technol. 312 (2017) 166–174.
[11] S. Pham-Ba, J.-F. Molinari, Creation and evolution of roughness on silica under unlubricated wear, Wear 472–473 (2021) 203648.
[12] H.C. Meng, K.C. Ludema, Wear models and predictive equations: their form and content, Wear 181–183 (1995) 443–457.
[13] R. Tarodiya, A. Levy, Surface erosion due to particle-surface interactions – A review, Powder Technol. 387 (2021) 527–559.
[14] M. Khanal, R. Morrison, Discrete element method study of abrasion, Miner. Eng. 21 (2008) 751–760.
[15] F. Fulchini, M. Ghadiri, A. Borissova, B. Amblard, S. Bertholin, A. Cloupet, M. Yazdanpanah, Development of a methodology for predicting particle attrition in a cyclone by CFD–DEM, Powder Technol. 357 (2019) 21–32.
[16] M. Ghadiri, Z. Zhang, Impact attrition of particulate solids. part 1: A theoretical model of chipping, Chem. Eng. Sci. 57 (17) (2002) 3659–3669.
[17] J.F. Archard, Contact and rubbing of flat surfaces, J. Appl. Phys 24 (1953) 981.
[18] I. Finnie, D.H. McFadden, On the velocity dependence of the erosion of ductile metals by solid particles at low angles of incidence, Wear 48 (1978) 181–190.
[19] H. Arabnejad, A. Mansouri, S.A. Shirazi, B.S. McLaury, Development of mechanistic erosion equation for solid particles, Wear 332–333 (2015) 1044–1050.
[20] D.G. Rickerby, N.H. Macmillan, On the oblique impact of a rigid sphere against a rigid-plastic solid, Int. J. Mech. Sci. 22 (8) (1980) 491–494.
[21] I.M. Hutchings, Deformation of metal surfaces by the oblique impact of square plates, Int. J. Mech. Sci. 19 (1) (1977) 45–52.
[22] M. Papini, J.K. Spelt, Impact of rigid angular particles with fully-plastic targets Part I: analysis, Int. J. Mech. Sci. 42 (5) (2000) 991–1006.
[23] M. Papini, J.K. Spelt, Impact of rigid angular particles with fully-plastic targets part II: Parametric study of erosion phenomena, Int. J. Mech. Sci. 42 (5) (2000) 1007–1025.
[24] Y. Ben-Ami, A. Levy, Absorbed shear energy during solid particle impact on ductile surface, Wear 368–369 (2016) 162–172.
[25] M.S. ElTobgy, E. Ng, M.A. Elbestawi, Finite element modeling of erosive wear, Int. J. Mach. Tool. Manu. 45 (11) (2005) 1337–1346.
[26] Y.F. Wang, Z.G. Yang, Finite element model of erosive wear on ductile and brittle materials, Wear 265 (5) (2008) 871–878.
[27] Z.G. Liu, S. Wan, V.B. Nguyen, Y.W. Zhang, A numerical study on the effect of particle shape on the erosion of ductile materials, Wear 313 (1) (2014) 135–142.
[28] M. Takaffoli, M. Papini, Material deformation and removal due to single particle impacts on ductile materials using smoothed particle hydrodynamics, Wear 274 (2012) 50–59.
[29] X.W. Dong, G.R. Liu, Z. Li, W. Zeng, A smoothed particle hydrodynamics (SPH) model for simulating surface erosion by impacts of foreign particles, Tribol. Int. 95 (2016) 267–278.
[30] V. Jardret, H. Zahouani, J.L. Loubet, T.G. Mathia, Understanding and quantification of elastic and plastic deformation during a scratch test, Wear 218 (1998) 8–14.
[31] K. Sun, L. Fang, Z. Yan, J. Sun, Atomistic scale tribological behaviors in nano-grained and single crystal copper systems, Wear 303 (1) (2013) 191–201.
[32] Y. Gao, A. Brodyanski, M. Kopnarski, H.M. Urbassek, Nanoscratching of iron: A molecular dynamics study of the influence of surface orientation and scratching direction, Comput. Mater. Sci. 103 (2015) 77–89.
[33] J. Bucaille, E. Felder, G. Hochstetter, Mechanical analysis of the scratch test on elastic and perfectly plastic materials with the three-dimensional finite element modeling, Wear 249 (5) (2001) 422–432.
[34] E. Felder, J.-L. Bucaille, Mechanical analysis of the scratching of metal sand polymers with conical indenters at moderate and large strains, Tribol. Int. 39 (2) (2006) 70–87.
[35] W.G. Hoover, C. Hoover, O. Kum, V. Castillo, H. Posch, S. Hess, Smooth Particle Applied Mechanics, World Scientific, 2006.
[36] S. Islam, R. Ibrahim, R. Das, T. Fagan, Novel approach for modelling of nano machining using a mesh-less method, Appl. Math. Model. 36 (11) (2012) 5589–5602.
[37] T. Rabczuk, T. Belytschko, Cracking particles: a simplified mesh-free method for arbitrary evolving cracks, Internat. J. Numer. Methods Engrg. 61 (13) (2004) 2316–2343.
[38] T. Rabczuk, E. Samaniego, Discontinuous modeling of shear bands using adaptive mesh-free methods, Comput. Methods Appl. Mech. Engrg. 197 (6–8) (2008) 641–658.
[39] S. Pham-Ba, J.-F. Molinari, Adhesive wear with a coarse-grained discrete element model, Comput. Methods Appl. Mech. Engrg. 397 (2022) 115124.
[40] R. Aghababaei, M. Malekan, M. Budzik, Cutting depth dictates the transition from continuous to segmented chip formation, Phys. Rev. Lett. 127 (2021) 235502.
[41] H. Huang, B. Lecampion, E. Detournay, Discrete element modeling of tool-rock interaction I: rock cutting, Int. J. Numer. Anal. Meth. 37 (2013) 1913–1929.
[42] S. Plimpton, Fast parallel algorithms for short-range molecular dynamics, J. Comput. Phys. 117 (1) (1995) 1–19.
[43] H.P. Zhang, H.A. Makse, Jamming transition in emulsions and granular materials, Phys. Rev. E 72 (2005) 011301.
[44] J.A. Williams, Analytical models of scratch hardness, Tribol. Int. 29 (8) (1996) 675–694.
[45] S. Zhang, X. Guo, Z. Jin, R. Kang, D. Guo, W.C. Tang, Surface morphologies and corresponding hardness evolution during nanoscratching, J. Mater. Res. Technol. 9 (3) (2020) 3179–3189.
[46] R. Capozza, K. Hanley, Raw Data for the Paper "A Comprehensive Model of Plastic Wear Based on the Discrete Element Method", Simulation Data, The University of Edinburgh, 2022, http://dx.doi.org/10.7488/ds/3440.
[47] C. Huang, S. Chiovelli, P. Minev, J. Luo, K. Nandakumar, A comprehensive phenomenological model for erosion of materials in jet flow, Powder Technol. 187 (2008) 273–279.
[48] R.G. Wellman, C. Allen, The effects of angle of impact and material properties on the erosion rates of ceramics, Wear 186–187 (1995) 117–122.
[49] Y.I. Oka, H. Olmogi, T. Hosokawa, M. Matsumura, The impact angle dependence of erosion damage caused by solid particle impact, Wear 203–204 (1997) 573–579.
[50] Y.I. Oka, K. Okamura, T. Yoshida, Practical estimation of erosion damage caused by solid particle impact: Part 1: Effects of impact parameters on a predictive equation, Wear 259 (1–6) (2005) 95–101.
[51] N. Vashishtha, S. Sapate, Effect of experimental parameters on wear response of thermally sprayed carbide based coatings, Mater. Res. 22 (1) (2019) 1–19.
[52] O. Noel, A. Vencl, P.-E. Mazeran, Exploring wear at the nanoscale with circular mode atomic force microscopy, Beilstein J. Nanotechnol. 8 (2017) 2662–2668.
[53] S.M. Hsu, M.C. Shen, Ceramic wear maps, Wear 200 (1996) 154–175.
[54] K. Adachi, K. Kato, N. Chen, Wear map of ceramics, Wear 203–204 (1997) 291–301.
[55] J.F. Archard, W. Hirst, The wear of metals under unlubricated conditions, Proc. R. Soc. Lond. Ser. A Math. Phys. Eng. Sci. 236 (1956) 397.
[56] A. Kareer, X.D. Hou, N.M. Jennett, S.V. Hainsworth, The existence of a lateral size effect and the relationship between indentation and scratch hardness in copper, Phil. Mag. 96 (2016) 3396–3413.
[57] A. Dasari, Z.-Z. Yu, Y.-W. Mai, Fundamental aspects and recent progress on wear/scratch damage in polymer nanocomposites, Mater. Sci. Eng. R 63 (2) (2009) 31–80.
[58] S. Leroch, M. Varga, S.J. Eder, A. Vernes, M. Rodriguez Ripoll, G. Ganzenmüller, Smooth particle hydrodynamics simulation of damage induced by a spherical indenter scratching a viscoplastic material, Int. J. Solids Struct. 81 (2016) 188–202.
[59] M. Varga, S. Leroch, S.J. Eder, M. Rodríguez Ripoll, Meshless microscale simulation of wear mechanisms in scratch testing, Wear 376–377 (2017) 1122–1129.
[60] K.J. Hanley, X. Huang, C. O'Sullivan, Energy dissipation in soil samples during drained triaxial shearing, Géotechnique 68 (2018) 421–433.